AIAA JOURNAL
Vol. 44, No. 4, April 2006

Direct Numerical Simulations of Transitional Supersonic Base Flows

Richard D. Sandberg* and Hermann F. Fasel†
University of Arizona, Tucson, Arizona 85721

Transitional supersonic base flows at $M = 2.46$ are investigated using direct numerical simulations. Results are presented for Reynolds numbers based on the cylinder diameter $Re_D = 3 \times 10^4$–1×10^5. As a consequence of flow instabilities, coherent structures develop that have a profound impact on the global flow behavior. Simulations with various circumferential domain sizes are conducted to investigate the effect of coherent structures associated with different azimuthal modes on the mean flow, in particular on the base pressure, which determines the base drag. Temporal spectra reveal that frequencies found in the axisymmetric mode can be related to dominant higher modes present in the flow. It is shown that azimuthal modes with low wave numbers cause a flat base pressure distribution and that the mean base pressure value increases when the most dominant modes are deliberately eliminated. Visualizations of instantaneous flow quantities and turbulence statistics at $Re_D = 1 \times 10^5$ show good agreement with experiments at a significantly higher Reynolds number. For these investigations, a high-order-accurate compressible Navier–Stokes solver in cylindrical coordinates developed specifically for this research was used.

Nomenclature

A	=	amplitude
c_p	=	pressure coefficient
c_v	=	specific heat
dt	=	computational time step
E	=	total energy, $E = c_v T + \frac{1}{2} u_i u_i$
K	=	turbulent kinetic energy
k	=	azimuthal Fourier mode number
L_K	=	Kolmogorov length scale
M	=	Mach number
n	=	temporal mode number
nr	=	number of radial gridpoints
nz	=	number of streamwise gridpoints
Pr	=	Prandtl number
p	=	pressure
$\boldsymbol{q}_k$	=	heat-flux vector
Re	=	Reynolds number
Sr	=	Strouhal number
T	=	temperature
t	=	time
u, v, w	=	velocity components in the streamwise, radial, and azimuthal direction
$\boldsymbol{u}_i$	=	velocity vector
$\langle u_i' u_k' \rangle$	=	turbulent stress tensor
W_{ik}	=	vorticity tensor
x_k	=	coordinate
z, r, θ	=	streamwise, radial, and azimuthal coordinates
γ	=	ratio of specific heats
Δ	=	computational grid size
δ_{ik}	=	Kronecker operator
ε	=	turbulent dissipation rate
μ	=	dynamic viscosity
τ_{ik}	=	stress tensor

Subscripts

D	=	quantity based on diameter of cylinder
i, j, k	=	indices for Cartesian tensor notation
in, out	=	inflow, outflow
max	=	maximum of referring quantity

Superscripts

k	=	kth mode of quantity
$'$	=	fluctuating quantity

Received 13 June 2005; revision received 18 September 2005; accepted for publication 3 October 2005.

*Research Fellow, Aerodynamics and Flight Mechanics Research Group, School of Engineering Sciences; currently Research Fellow, School of Engineering Sciences, University of Southampton, Southampton, England SO17 1BJ, United Kingdom; sandberg@soton.ac.uk. Member AIAA.

†Professor, Department of Aerospace and Mechanical Engineering; faselh@email.arizona.edu. Member AIAA.

I. Introduction

FLIGHT vehicles at supersonic speed ideally are fitted with a streamlined afterbody to avoid a large drag force. In many practical applications, ranging from projectiles to missiles, however, it is not possible to implement such an aerodynamic improvement. For example, most tactical and defense missiles spend a considerable portion of their flight coasting, where the burnt out rocket motor presents a blunt base to the flow. A recirculation region forms behind the base of the body that is responsible for a low base pressure, thus causing aerodynamic drag (base drag). Flight tests with projectiles (U.S. Army 549 projectile) have shown that the base drag may account for up to 35% of the total drag.[1] Simulations performed for artillery shells at $M = 0.9$ showed that the base drag can even account for up to 50% of the total aerodynamic drag.[2] The total drag determines the range, terminal velocity, or the payload of the object, thus playing a crucial role in the design process.

Because of the large contribution of the base drag to the overall drag, modifying the near-wake region such that the base pressure would increase could be highly rewarding with respect to drag reduction and, as a consequence, increasing the performance characteristics of flight vehicles or projectiles. However, to modify the near-wake flow effectively, the fundamental physical mechanisms that govern the development and evolution of coherent structures in the wake, leading to an alteration of the base pressure, need to be understood. Only then can efficient modifications of the near wake be implemented in the form of passive control such as base bleed,[2–9] boattailing,[10–12] base burning,[13,14] etc., or, eventually, even active flow control.

It is well known that for subsonic (incompressible) wakes, the dynamics of the large coherent structures play a dominant role in the local and global behavior of the flow. At supersonic speeds,

however, very little is known about the dynamic behavior of large coherent structures and their effect on the base drag. Early measurements of turbulence in an axisymmetric compressible wake that indicate the existence of dominant large structures include the work by Demetriades.[15–17] Amplitude spectra (Figs. 11–14 in Ref. 16) displayed distinct peaks at relatively low frequencies, thus indicating the presence of dominant modes (structures). In addition, amplitude distributions for the velocity fluctuations (Figs. 2 and 3, respectively, in Ref. 16) resembled that of an incompressible axisymmetric wake, where it is known that the resulting profile is due to the presence of dominant, large coherent structures (cf. Cannon and Champagne[18]). More recently, with the emergence of new experimental techniques, it could be verified that large-scale structures exist in supersonic base flows. In carefully designed experiments of supersonic base flows at $M = 2.46$ and $Re_D = 3.3 \times 10^6$ at the UIUC, planar visualizations showed evidence of the existence of large, coherent turbulent structures, that is, with their size on the order of the shear-layer thickness.[19–21] However, even though large coherent turbulent structures were shown to exist, their origin and impact on the mean flow are far from understood. The high speeds of the flows make it very difficult to acquire experimentally time-dependent data with the necessary temporal resolution to track individual structures and get clues about their origin and evolution. Therefore, complementary numerical simulations might offer valuable insights into the physical mechanisms relevant in the near-wake region.

Numerous computational efforts have been made to investigate supersonic base flows.[2,22–27] However, the focus of most of these investigations has mainly been on matching steady mean flow data from the experiments by Dutton and coworkers. No significant effort has been made on identifying and understanding the dynamic behavior of the large-scale vortical structures and their effect on the mean flow. The main reasons for this are certainly the relatively high Reynolds number of the experiments and that three-dimensional calculations are required because the large structures are three-dimensional for the Mach number under investigation. As a consequence, the high-resolution requirements prohibit fully resolved DNS of the high-Reynolds-number conditions of the experiments. Other simulation strategies that capture all of the relevant physics of fully turbulent supersonic base flows are still in the development stage and have yet to be entrusted with stability investigations.

Recently, Sandberg and Fasel[28] took advantage of the ability of numerical simulations to deliberately exclude physical effects and, therefore, assess their importance. They performed linear stability analysis with complementary spatial and temporal DNS to identify the fundamental hydrodynamic mechanisms leading to the generation of large structures. The focus of the current paper is to shed light on the effect of the large structures on the mean flow, in particular on the base pressure. The method of choice is to conduct stability investigations of transitional supersonic base flows using DNS. Although for the Reynolds numbers chosen the flow is not fully turbulent, it was shown previously that many of the qualitative features found in the UIUC experiments can be captured.[29,30] Moreover, transitional flows facilitate the investigation of the initial development of the large-scale structures because the breakdown to small-scale turbulence either does not fully occur or takes place on a relatively slow timescale, leading to a well-defined separation of scales. For the current work, it is further sought to exploit the strength of numerical experiments to exclude certain physical effects. This is achieved by conducting DNS of various circumferential domain sizes. Thus, different azimuthal modes can deliberately be eliminated and their influence on the global flow behavior can be evaluated. Temporal spectra mean flow data, including base pressure distributions and turbulence statistics, are presented for various circumferential domain sizes at Reynolds numbers $Re_D = 3 \times 10^4$–10^5 and $M = 2.46$. A comparison of the results obtained from direct numerical simulation (DNS) with the University of Illinois at Urbana–Champagne (UIUC) experiments is discussed.

II. Governing Equations

The flow under consideration is governed by the full compressible Navier–Stokes equations in cylindrical coordinates. The fluid is assumed to be an ideal gas with constant specific heat coefficients. All quantities are made dimensionless using the flow quantities at a reference location in the flow; here the freestream/inflow location is used. The radius of the body was chosen as the reference length. For simplicity, all equations in this section are presented in tensor notation. The nondimensional continuity, momentum, and the energy equations are

$$\frac{\partial \rho}{\partial t} + \frac{\partial}{\partial x_k}(\rho u_k) = 0 \tag{1}$$

$$\frac{\partial}{\partial t}(\rho \boldsymbol{u}_i) + \frac{\partial}{\partial x_k}[\rho \boldsymbol{u}_i u_k + p\delta_{ik} - \tau_{ik}] = 0 \tag{2}$$

$$\frac{\partial}{\partial t}(\rho E) + \frac{\partial}{\partial x_k}\left[\rho u_k\left(E + \frac{p}{\rho}\right) + q_k - \boldsymbol{u}_i \tau_{ik}\right] = 0 \tag{3}$$

The stress tensor and the heat-flux vector are computed as

$$\tau_{ik} = \frac{\mu}{Re}\left(\frac{\partial \boldsymbol{u}_i}{\partial x_k} + \frac{\partial u_k}{\partial x_i} - \frac{2}{3}\frac{\partial u_j}{\partial x_j}\delta_{ik}\right) \tag{4}$$

$$\boldsymbol{q}_k = \frac{-\mu}{(\gamma - 1)M^2 Pr Re}\frac{\partial T}{\partial x_k} \tag{5}$$

respectively, where μ is computed according to Sutherland's law, $\gamma = 1.4$, and $Pr = 0.7$. To close the system of equations, the pressure is obtained from the nondimensional equation of state $p = (\rho T)/(\gamma M^2)$.

III. Numerical Method

A. General Features of the Code

The compressible Navier–Stokes equations in cylindrical coordinates are solved using sixth-order accurate split compact differences for the radial direction and fourth-order accurate split differences in the streamwise direction. To preserve accuracy, the finite differences are derived for nonequidistant grids.[31] High-order accurate finite differences were chosen to avoid excessive numerical dissipation and phase errors and, therefore, ensure a clean environment for the investigation of instabilities. The computational domain is shown in Fig. 1. Grid stretching was employed for the radial and the streamwise directions to provide adequate spatial resolution in regions of high gradients, for example in the approach flow boundary layer, the shear layer, and the corner of the afterbody. Note that the accuracy of high-order finite difference schemes suffers significantly once the grid is very strongly stretched.[32] Therefore, in the radial direction the grid was designed to be equidistant behind the base, $0 \le r \le 1$, to achieve the highest possible accuracy. By the same token, a large number of grid points was used in the streamwise direction to enforce a benign grid stretching with ratios of $\Delta z_{\max}/\Delta z_{\min} \le 20$. The axisymmetric wake is a natural application for the use of a spectral discretization in the azimuthal direction due to the periodicity of the physical problem. For that reason, a pseudospectral approach in the azimuthal direction was chosen. Because of the use of symmetric

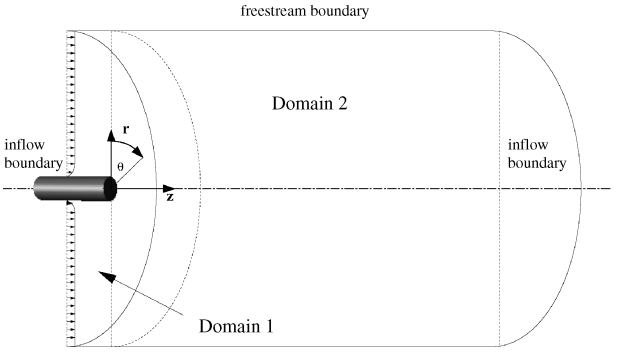

Fig. 1 Computational domain for one-half-cylinder case.

Fourier transforms, the magnitudes and distributions of azimuthal Fourier modes k and $-k$ are identical. Therefore, throughout the remainder of this paper, we will not distinguish between positive and negative modes. For simplicity the technically correct notation of $k = \pm 1, \pm 2, \ldots, \pm k_{\max}$ is replaced by $k = 1, 2, \ldots, k_{\max}$. For the time advancement, a standard fourth-order accurate Runge–Kutta scheme is employed. A domain decomposition was implemented in the streamwise direction for efficient parallelization.

B. Axis Treatment

Because of the pseudospectral approach in the azimuthal direction, the flowfield is given at every time step in Fourier modes, with the zeroth mode being the azimuthal mean flow. A state-of-the-art axis treatment is implemented, exploiting parity conditions. Even parity implies that the even azimuthal modes of a variable have an even symmetry, and the odd modes have an odd symmetry at the axis. For odd parity, the even azimuthal modes of the variable have an odd symmetry and the odd modes have an even symmetry at the axis. The quantities ρ, u, and E have even parity and v and w have odd parity in the one-half-cylinder case.[33] The boundary conditions at the axis are as follows: The zeroth azimuthal mode of all quantities evolve according to the governing equations; only the radial and azimuthal velocity are set to zero. The first mode of the radial and azimuthal velocity components are permitted to be nonzero at the axis; however, all other higher modes are set to zero at the axis.

A modification of this axis treatment had to be implemented to allow for calculations of domains with an azimuthal extent of less than π. In the case of a one-quarter-cylinder, the calculation contains only the azimuthal modes $2, 4, 6, \ldots, k_{\max}$; hence, all higher modes must be set to zero at the axis in contrast to the one-half-cylinder case. Also, for the one-quarter-cylinder case, the parity conditions need to be changed, because all modes are even. For the option of computing $1/8$ or $1/16$ of a cylinder, only the modes $k = 4, 8, 12, \ldots, k_{\max}$ or $k = 8, 16, 24, \ldots, k_{\max}$ are computed, respectively, requiring the same axis treatment as for the one-quarter-cylinder case. The one-sixth-cylinder case poses an exception, allowing for modes $k = 3, 6, 9, \ldots, k_{\max}$ and thereby containing even and odd modes. This case can be treated like the one-half-cylinder case in terms of the parity conditions at the axis. However, because the first mode is not included, the boundary condition at the axis is the same as for all other domain sizes with $\theta < \pi$.

Further details on the spatial and temporal discretization and a listing of all boundary conditions and symmetry conditions at the axis, are given by Sandberg.[34] The numerical procedure was thoroughly validated with various test cases by Sandberg and selected results were published by Sandberg and Fasel.[30]

IV. Results

Initially, axisymmetric simulations, that is, the r–z plane for the zeroth azimuthal mode only, for a range of Reynolds numbers were conducted for several different computational grids to determine the necessary grid resolution. The approach boundary layer was designed such that, for all cases, the boundary-layer thickness at the separation point was $\delta_c = 0.1R$, matching the data from the UIUC experiments. The axisymmetric calculations converged to a steady solution for all Reynolds numbers investigated here, implying that no absolute instability with respect to axisymmetric disturbances is present for these Reynolds numbers. This was confirmed with linear stability analysis by Sandberg and Fasel.[28] The three-dimensional simulations were then initialized with the zeroth azimuthal mode set to the converged axisymmetric flowfields and the higher modes set to zero. A pulse disturbance was introduced into the higher modes of density downstream of the base within the recirculation region. For all cases, the approach flow was laminar, and transition to turbulence occurred downstream of the separation point.

All DNS were conducted at the Mach number of the UIUC experiments, $M = 2.46$. The lowest Reynolds number investigated was $Re_D = 3 \times 10^4$, allowing for a reasonable turn-around time due to the moderate resolution requirements, albeit exhibiting an absolute instability with respect to the higher azimuthal modes leading to the development of large structures.[28] Linear stability calculations showed a significant increase in the growth rates of disturbances at $Re_D = 6 \times 10^4$ compared to lower Reynolds numbers, in particular for the higher azimuthal modes.[28,34] Therefore, simulations were conducted at $Re_D = 6 \times 10^4$ to evaluate whether a significant change in the wake behavior would occur. The largest Reynolds number chosen was $Re_D = 1 \times 10^5$ because this constituted the highest Reynolds number possible with the resources available at the time of this research. For all Reynolds numbers investigated, the distance from the inflow boundary to the outflow boundary was $z_{\text{out}} - z_{\text{in}} > 11$, and the freestream boundary was located at $r_{\max} = 6$. The number of streamwise and radial points and Fourier modes used to discretize the computational domain for a half-cylinder case, $0 \le \theta \le \pi$, and the finest grid spacing at the base corner along with the computational time step for the three Reynolds numbers investigated are given in Table 1. The time step was determined by globally satisfying the diffusion or Courant–Friedrichs–Lewy (CFL) limit, whichever was more restrictive to ensure time-accurate results. The resolution in the azimuthal direction was considered adequate if a considerable decay of energy over the azimuthal modes could be found (at least three orders of magnitude compared with the first mode). To ensure convergence of the results, the calculation at $Re_D = 3 \times 10^4$ was repeated with a considerably finer grid ($3 \times 10^4 f$ in Table 1). Mean flow results compared for both grids were virtually indistinguishable, implying that the coarser grid resolution was sufficient. Once it was verified that the grid resolution was adequate, simulations of integration domains with an azimuthal extent of $\theta < \pi$ were also conducted, deliberately suppressing various modes of the half-cylinder case. The number of Fourier modes for the calculations with smaller circumferential domain sizes were chosen such that the azimuthal resolution remained constant. For example, if the $1/2$-cylinder calculation was performed with 64 modes, then 32, 24, 16 and 8 modes were used for the $1/4$-cylinder, $1/6$-cylinder, $1/8$-cylinder, and the $1/16$-cylinder calculations, respectively. Note that in the following text, the mode numbers denoted by k refer to the corresponding positive and negative mode numbers in the half-cylinder case, not the computational mode of the respective calculation, that is, mode $k = 2$ always has a wavelength of π, for example.

Table 1 Number of points in streamwise *nz* and radial direction *nr* and number of Fourier modes *k* used for discretizing computational domain

Re_D	nz	nr	$k_{\max}$	$\Delta\,(z, r)_c$[a]	dt[b]
3×10^4	452	130	32	0.01	1.5×10^{-3}
$3 \times 10^4 f$	520	200	64	0.008	1.19×10^{-3}
6×10^4	812	130	128	0.01	1.375×10^{-3}
1×10^5	1272	160	128	0.008	8.0×10^{-4}

[a]Finest grid spacing at corner. [b]Computational time step.

A. Temporal Spectra

The pulse response of the higher azimuthal density modes at the disturbance location was monitored for all cases investigated. Rapid growth was observed for all domain sizes, implying that the flow is absolutely unstable with respect to modes $k = 1$–8. An interval of the temporal development of the Fourier modes of density in a region of high activity, here the recompression region, is shown for the cases at $Re_D = 3 \times 10^4$ in Figs. 2a–2d. The initial startup transient is already overcome, and a fully nonlinear saturation level has been reached. The decay in energy over the azimuthal modes amounts to approximately three orders of magnitude for the four largest domain sizes and even more for the $1/16$-cylinder, suggesting that the resolution in the azimuthal direction is sufficient. For the fine grid calculation at $Re_D = 3 \times 10^4$ (not shown here), the amplitude of the highest mode $k = 64$ was close to five orders of magnitude smaller than the first mode.

For the one-half-cylinder case (Fig. 2a) the magnitude all modes decays between $80 < t < 100$, leading to a relatively quiet region in the interval $100 < t < 110$. This is a strong indication that the flow is intermittent at this Reynolds number. This behavior was also

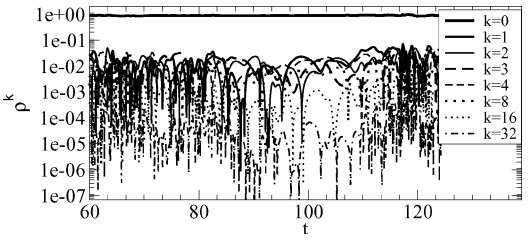

a) 1/2-cylinder

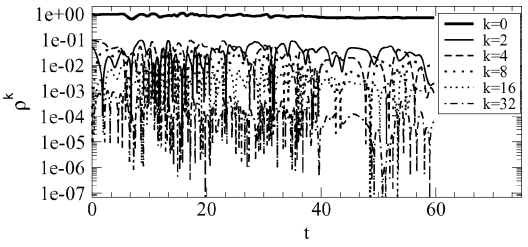

b) 1/4-cylinder

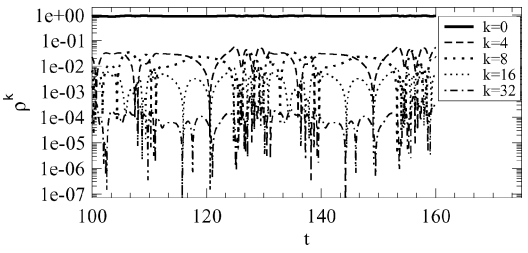

c) 1/8-cylinder

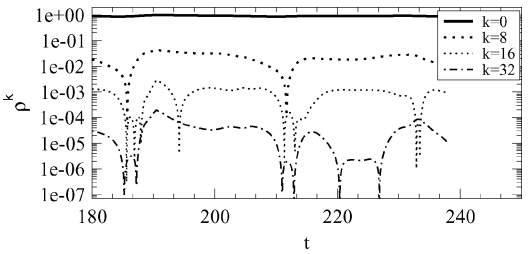

d) 1/16-cylinder

Fig. 2 Temporal development of Fourier modes of ρ in a region of high activity: $z = 4.82$, $r = 0.238$, $Re_D = 3 \times 10^4$, and $M = 2.46$.

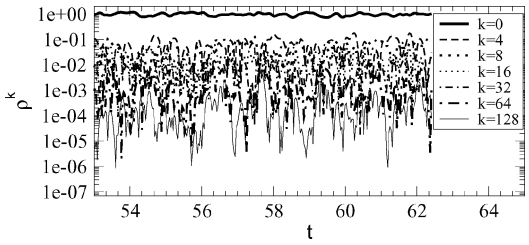

a) $Re_D = 6 \times 10^4$, 1/8-cylinder

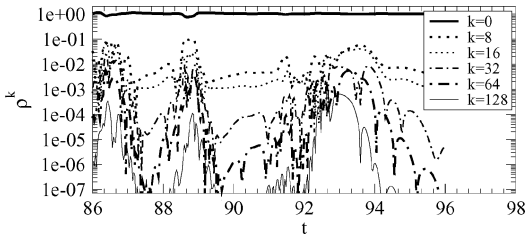

b) $Re_D = 6 \times 10^4$, 1/16-cylinder

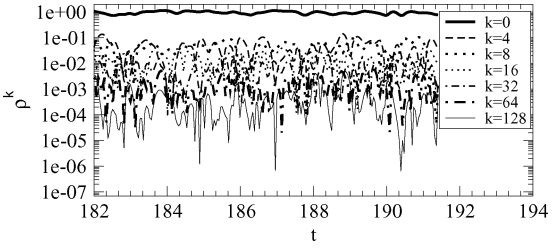

c) $Re_D = 1 \times 10^5$, 1/8-cylinder

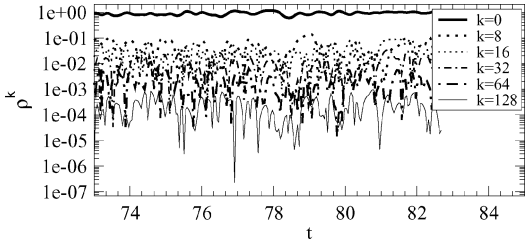

d) $Re_D = 1 \times 10^5$, 1/16-cylinder

Fig. 3 Temporal development of Fourier modes of ρ in a region of high activity; $z = 7.85$, $r = 0.465$ ($Re_D = 6 \times 10^4$) and $z = 8.27$, $r = 0.336$ ($Re_D = 1 \times 10^5$), and $M = 2.46$.

found for subsonic wakes at $Re_D = 10^3$ that were conducted as validation cases.[30] The presence of intermittency for the current case at a significantly higher Reynolds number illustrates the damping effect of compressibility. A possible explanation for the occurrence of intermittency is proposed: The axisymmetric mean flow is unstable and gives rise to primary instabilities, which, in turn, lead to secondary and tertiary instabilities that cause the formation of large- and small-scale structures. The large-scale structures interact nonlinearly with the mean flow to an extent that the resulting mean flow is no longer unstable, which, as a consequence, leads to a quiet region. Once the large structures are convected downstream and the mean flow becomes unstable again, disturbances can again be amplified, resulting in the repeated generation of large- and small-scale structures.

The same behavior was observed for the one-quarter-cylinder case (Fig. 2b) and the one-sixth-cylinder case (not shown), that is, the flow displays intermittency, particularly noticeable in the interval $130 < t < 142$. For the one-eighth-cylinder (Fig. 2c), the graph changes drastically, showing far smaller amplitudes in the higher modes, and the fraction of quiet regions increases. This behavior is even more pronounced in the $1/16$-cylinder case (Fig. 2d) where the flow fails to exhibit any high-frequency oscillations. The fact that the smaller circumferential domain sizes do not exhibit high-frequency oscillations is attributed to a viscous cutoff, that is, the highest modes are damped by viscous diffusion. Therefore, at this fairly low Reynolds number, the highest wave numbers do not reach large amplitudes by themselves. Also, the exclusion of low wave number modes, which are highly unstable, inhibits an energy cascade to the higher wave numbers, resulting in the absence of small-scale structures.

Figures 3a–3d show the temporal development of the Fourier modes for the $1/8$-cylinder and $1/16$-cylinder cases at $Re_D = 6 \times 10^4$ and 1×10^5. Note that only intervals of 12 time units are shown in contrast to 60 time units for the $Re_D = 3 \times 10^4$ cases, due to smaller timescales present. The results for the larger domain sizes for both Reynolds numbers are highly similar to the one-eighth-cylinder case of the respective Re_D, that is, no intermittency can be observed, and high-frequency oscillations are found. Therefore, these cases are not shown to maintain conciseness of the paper. For the $1/16$-cylinder case at $Re_D = 6 \times 10^4$ (Fig. 3b) the flow appears to be intermittent; however, it still features high-frequency oscillations in time in contrast to this domain size at the lower Reynolds number. In addition, the amplitudes of the higher modes are several orders of magnitude smaller than for the larger domain sizes. Only at $Re_D = 1 \times 10^5$, even the smallest domain size computed shows no sign of intermittency and displays high-frequency oscillations. This implies that the increased Reynolds number has shifted the

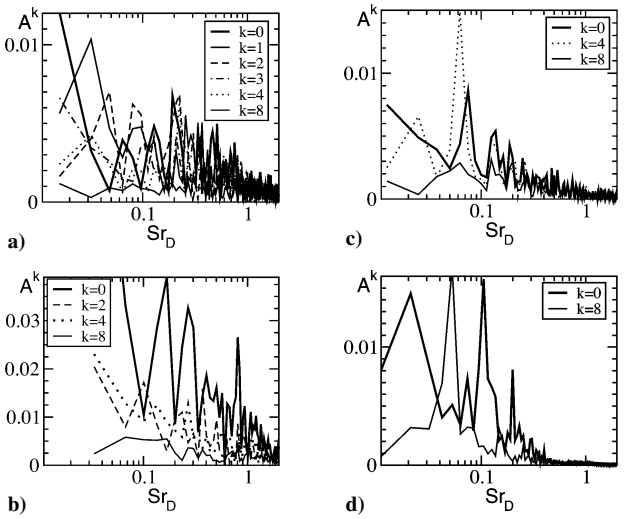

Fig. 4 Fourier decomposition in time of higher density modes in region of high activity: a) 1/2-cylinder, b) 1/4-cylinder, c) 1/8-cylinder, and d) 1/16-cylinder; $z = 4.82$, $r = 0.238$, $Re_D = 3 \times 10^4$, and $M = 2.46$.

viscous cutoff to considerably higher wave numbers. In addition, significant temporal variations of the azimuthal mean $k = 0$ at the probe point can be observed, indicating that the amplitudes of the azimuthal modes are sufficiently large to cause considerable nonlinear interaction with the zeroth mode.

The data of the azimuthal Fourier modes of density in the recompression region (for a much larger time interval than shown in Figs. 2 and 3) were Fourier decomposed in time. The frequency spectra obtained were scrutinized to identify dominant frequencies in the flow. As shown, in several cases the flow exhibits an intermittent behavior. This complicated the Fourier analysis in time, and a study of how the size of the sampling interval would affect the resulting frequency spectrum was conducted. In conclusion, postprocessing only a smaller interval led to more distinguished peaks and facilitated the identification of dominant frequencies. However, when the entire data set was Fourier transformed, the same dominant frequencies (for Strouhal numbers based on diameter $Sr_D > 0.1$) could still be detected, with the benefit of including additional information in the low-frequency range. Therefore, for all cases, all data were used for the temporal Fourier decomposition.

The amplitudes of selected azimuthal Fourier modes over the Strouhal number at $Re_D = 3 \times 10^4$ are shown for all circumferential domain sizes, except the one-sixth-cylinder, in Fig. 4. For the half-cylinder case, it can be observed that modes $k = 1, 2, 3$, and 4 contain most of the energy. Modes $k = 1$ and $k = 4$ exhibit a very strong peak at $Sr_D = 0.031$. When a dominant frequency is denoted as temporal mode n, the nonlinear interaction of (n, k) with itself can result in either a response of the azimuthal mean with twice the frequency, $(n, k) + (n, -k) = (2 \times n, 0)$, or a higher azimuthal mode with twice the frequency $(n, k) + (n, k) = (2 \times n, 2 \times k)$. Here, it appears as if the nonlinear interaction results in a peak with twice the frequency in the azimuthal mean flow $k = 0$. This can be validated by detecting that this peak in $k = 0$ does not exist in the cases where mode $k = 1$ was omitted. At $Sr_D = 0.08$, peaks in both $k = 1$ and 2 coincide. This value is similar to the frequency observed for a slow lateral motion (flapping) of the entire wake in the r–z plane at $\theta = 0, \pi$ which, therefore, can be attributed to these two modes. Furthermore, mode $k = 2$ exhibits multiple peaks at moderate frequencies, coinciding with mode $k = 4$ at $Sr_D = 0.22$, suggesting that these two modes are causing large structures in the recompression region. For higher Sr_D, the frequencies of the peaks for the mean flow $k = 0$ cannot be expressed in multiples of isolated higher modes, implying that the modification of the mean flow is caused by simultaneous nonlinear interaction of several higher modes.

In the one-quarter-cylinder case, there is again evidence that strong structures are present, considering the large amplitudes of the lower modes at low frequencies. Modes $k = 2$ and 4 exhibit the most prominent peaks. The azimuthal mean flow ($k = 0$) shows several peaks at low frequencies but also exhibits a distinctive maximum at $Sr_D \approx 0.8$, nonlinearly generated by $k = 2$. The large amplitudes found for the zeroth mode in this case might be due to the elimination of the first mode. The higher modes cannot interact with $k = 1$ or any other odd mode. Therefore, a significant energy exchange appears to take place directly with the azimuthal mean. For brevity, the results of the one-sixth-cylinder simulation are not shown here. However, a discussion of the data was published in Sandberg and Fasel.[35]

The one-eighth-cylinder case reveals a peak of mode $k = 4$ at $Sr_D = 0.022$, which denotes the frequency of the vortex shedding. Also, a very prominent maximum can be seen at $Sr_D = 0.06$ for the same mode, possibly generating a peak in mode $k = 8$ for the same Strouhal number through a nonlinear interaction with itself. Both modes seem to produce a peak in the zeroth mode at twice the frequency, that is, $Sr_D = 0.12$. For the 1/16-cylinder case, the graph simplifies drastically because only one mode appears to interact with the circumferential mean flow. Mode $k = 8$ exhibits only one noticeable peak at $Sr_D = 0.05$, nonlinearly interacting with itself and producing a reaction of the mean flow $k = 0$ for twice ($Sr_D = 0.1$) the frequency. Mode $k = 0$ then nonlinearly interacts with itself to produce a peak at $Sr_D = 0.2$. When snapshots of instantaneous vorticity magnitude are scrutinized for this case, an absence of structures with varying length scales can be detected. The lack of small-scale structures for the small domain sizes most likely can be attributed to the afore mentioned viscous cutoff of the high wave number modes. For the larger domain sizes, modes with longer wavelengths are unstable and reach large amplitudes, nonlinearly generating higher wave numbers and, thus, producing small-scale structures.

The Fourier decomposition of the time signal for several domain sizes at $Re_D = 6 \times 10^4$ is shown in Fig. 5. In contrast to the $Re_D = 3 \times 10^4$ cases, it is evident that a significant amount of energy is contained in frequencies with $Sr_D \geq 1$. In the one-half-cylinder case, mode $k = 1$ shows a prominent peak at $Sr_D = 0.175$. This value is noticeably higher than for the $Re_D = 3 \times 10^4$ case ($Sr_D = 0.08$). Structures with this frequency have a great effect on the azimuthal mean flow, evidenced by the peak of $k = 0$ at twice the frequency $Sr_D = 0.35$. Modes $k = 2$ and 4 appear to have the largest impact on the azimuthal mean in the lower frequency range for the one-quarter-cylinder case, displaying several peaks at $Sr_D < 1$. For larger Strouhal numbers, mode $k = 2$ appears to be the dominant higher mode. However, for this region no further assumptions can be made about which modes have the most pronounced effect on mode $k = 0$. It can only be observed that the mean flow possesses a dominant frequency with $Sr_D = 1.63$.

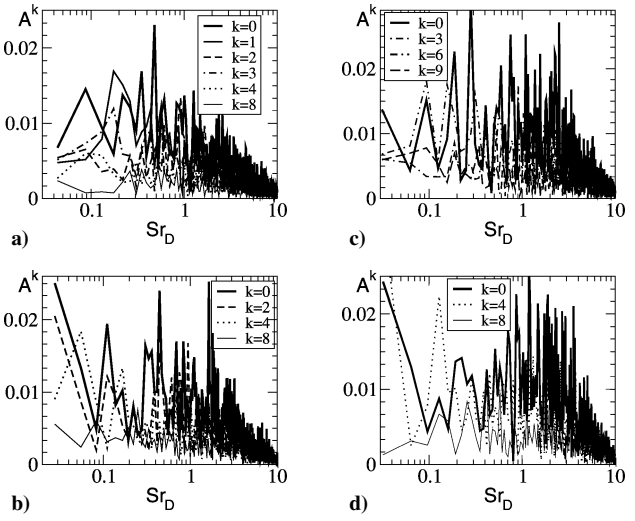

Fig. 5 Fourier decomposition in time of higher density modes in a region of high activity: a) one-half cylinder, b) one-quarter cylinder, c) one-sixth-cylinder, and d) one-eighth-cylinder; $z = 7.85$, $r = 0.465$, $Re_D = 6 \times 10^4$, and $M = 2.46$.

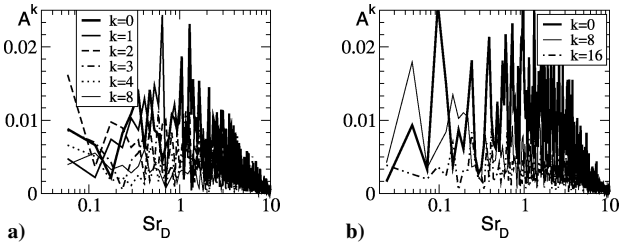

Fig. 6 Fourier decomposition in time of higher density modes in a region of high activity: a) 1/2-cylinder and b) 1/16-cylinder; $z = 8.27$, $r = 0.336$, $Re_D = 1 \times 10^5$, and $M = 2.46$.

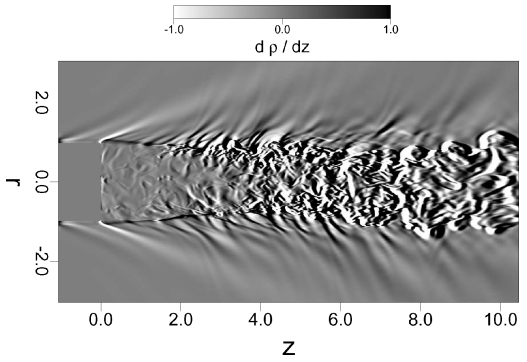

Fig. 7 Instantaneous streamwise density gradient: $Re_D = 1 \times 10^5$ and $M = 2.46$.

In contrast to the lower-Reynolds-number case, for the one-sixth-cylinder case the largest amount of energy is contained in $k = 3$. A significant maximum of $k = 3$ at $Sr_D = 0.09$ coincides with $k = 9$ and nonlinearly generates a peak in the azimuthal mean at the same frequency. It is likely that this maximum of $k = 3$ is responsible for a higher harmonic of $k = 0$, 6, and 9 at $Sr_D = 0.18$. The global maximum of $k = 0$ found at $Sr_D = 0.28$ appears to be generated by the third mode as well, which shows a pronounced peak at $Sr_D = 0.14$. The one-eighth-cylinder case is dominated by modes $k = 4$ and 8, which exhibit strong peaks at frequencies as high as $Sr_D = 5$ with significant nonlinear effects on the azimuthal mean. Mode $k = 4$ has its most prominent maximum at $Sr_D = 0.12$, which is double the frequency of that found in the lower-Reynolds-number case.

The Fourier decomposition of the time signals at $Re_D = 1 \times 10^5$ are shown in Fig. 6. As at $Re_D = 6 \times 10^4$, it is evident that a significant amount of energy is contained in frequencies with $Sr_D \geq 1$, here even for the 1/16-cylinder case. For the one-half-cylinder case, mode $k = 1$ shows a local maximum at a slightly higher Strouhal number ($Sr_D = 0.19$) than at $Re_D = 6 \times 10^4$. A prominent peak in the first mode, however, can be found at a noticeably higher Strouhal number of 0.62. Structures with this frequency seem to have a great effect on the azimuthal mean flow, evidenced by the peak of $k = 0$ at twice the frequency, $Sr_D = 1.24$. In addition, mode $k = 4$ displays multiple peaks in both the high- and low-frequency range. The results from the smaller domain sizes are similar to the respective domain sizes at $Re_D = 6 \times 10^4$ and are omitted here for brevity. Only the data from the 1/16-cylinder case are shown to illustrate the broad range of frequencies for modes $k = 0$, 8, and 16. The most pronounced peak for $k = 8$ is found at $Sr_D = 0.05$, creating the largest amplitudes in $k = 0$ at twice the frequency ($Sr_D = 0.1$).

To illustrate the topology of the flowfield, instantaneous streamwise density gradients are shown for the one-half-cylinder case at $Re_D = 1 \times 10^5$ in Fig. 7. The most prominent features of the flow are visible: A laminar boundary layer separates at the base corner, causing an expansion fan. A thin free shear layer is formed, separating the outer inviscid fluid from a large recirculation region downstream of the base. First large-scale structures develop at approximately 1 radius downstream of the base, as evidenced by shocklets. The pseudo-schlieren visualization also reveals the recompression shock system that realigns the shear layer with the axis. The occurrence of large, coherent structures is apparent. In fact, a broad range of large- and small-scale structures can be observed, causing a significantly decreased recirculation length, as will be shown when mean flow results are discussed later.

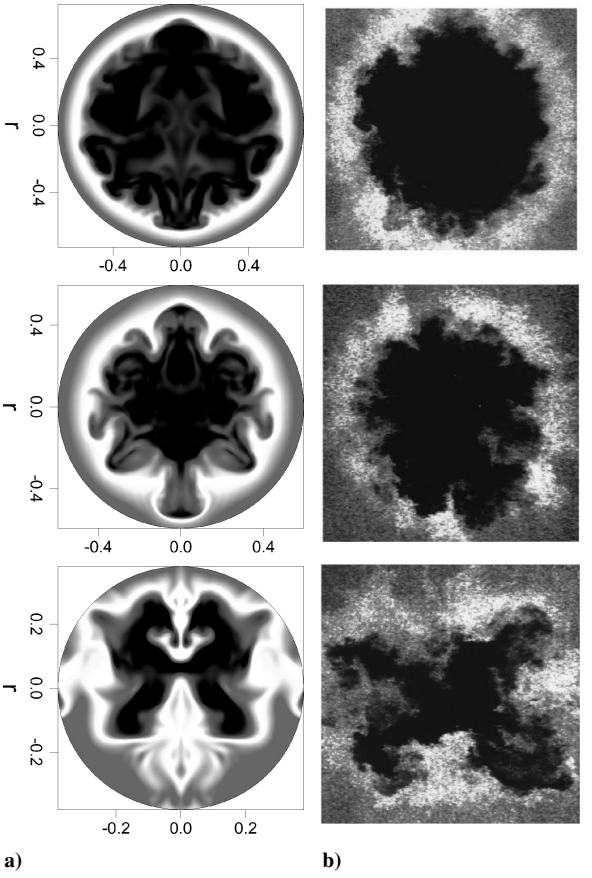

Fig. 8 End views of contours of instantaneous local Mach number: a) $Re_D = 1 \times 10^5$ and $M = 2.46$, compared with from experiment by Bourdon and Dutton,[19] and b) $Re_D = 3.3 \times 10^6$ and $M = 2.46$; location snapshots C, D, and E are shown from top to bottom.

With the flow transitioning rapidly after separation and displaying a broad range of length and timescales, a comparison to the (higher-Reynolds-number) UIUC case is attempted. In experiments by Bourdon and Dutton,[19] the identification of coherent structures was achieved through a Mie-scattering technique. Condensing ethanol vapor was illuminated with planar laser sheets, and high-speed snapshots were taken to obtain instantaneous visualizations of large-scale structures. To compare data obtained from DNS with the experimental data, contours of instantaneous local Mach number were chosen for visualization. End views of DNS data are shown in Fig. 8 for the streamwise positions $z = 3.5$, 4.0, and 6.5, which are qualitatively similar to locations C, D, and E in Ref. 19, respectively. At the location upstream of mean reattachment, $z = 3.5$, mushroomlike structures can be detected within the inside of the shear layer. These structures strongly resemble those visualized in the experiments at a comparable location (C) and indicate the existence of streamwise vortices within the shear layer. Over a longer time interval, approximately 12–14 mushroomlike structures could be observed instantaneously, in good agreement with the typical number of 10–14 observed in the experiment. The streamwise location $z = 4.0$ is within the recompression region and corresponds to position D in the experiments. Here, the number of instantaneous mushroom-shaped structures has reduced to roughly 8–10 structures, comparable with the number of vortices observed at UIUC. This indicates that the streamwise structures undergo an amalgamation in the streamwise direction that intuitively seems inevitable in light of the lateral convergence of the shear layer. In the developing wake, at $z = 6.5$ (corresponding to location E in the experiments), only four structures are visible for some instances, as was also the

Fig. 9 Instantaneous perspective view of $|W_{ik}| = 5$ for one-half-cylinder case: $Re_D = 1 \times 10^5$ and $M = 2.46$.

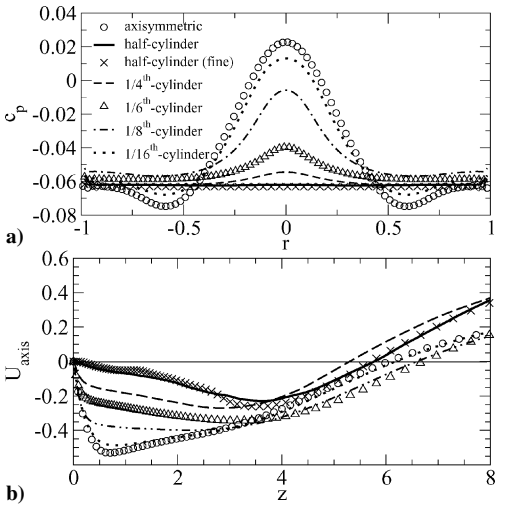

Fig. 10 All circumferential domain sizes: a) averaged pressure coefficient and b) streamwise axis velocity, $Re_D = 3 \times 10^4$ and $M = 2.46$.

case in the experiments. This four-lobe structure is a strong indication that modes $k = 2$ and 4 might be the dominant modes in the developing wake. That this is indeed the case was confirmed with end views and radial amplitude distributions of the mean flow.[28] The off-center location of the wake hints at a flapping motion, most likely caused by mode $k = 1$. Because of the strong similarities between the DNS results and the experimental data, it is conjectured that the same instability mechanisms are present. It is, therefore, proposed that modes $k = 2$ and 4 might also be dominant in the high-Reynolds-number case investigated at UIUC. The visualization of isosurfaces of vorticity magnitude $|W_{ik}| = 5$ (Fig. 9) confirms the presence of streamwise vortices within the shear layer, which are responsible for the mushroom-shaped structures observed in the end views. It appears that the streamwise structures do not persist throughout the recompression region. Instead, they break up, forming a considerable number of hairpin vortices downstream of the recompression region. Nevertheless, this does not exclude the occurrence of a four-lobe wake structure, as seen in Fig. 8. The small-scale structures merely cause an additional modulation of the lobes.

B. Mean Flow

To assess the impact of the large-scale structures on the mean flow, averaged flow quantities need to be evaluated. To obtain time averages, the DNS were conducted until running averages were converged, which required approximately 12 flow-through times for all cases. End views and radial amplitude distributions of the mean flow were analyzed by Sandberg and Fasel,[28,29] Sandberg,[34] and Sandberg and Fasel[35] and are not shown here for brevity. It was concluded that the azimuthal modes $k = 2$ and 4 were most dominant in the one-half-cylinder cases for all Reynolds numbers investigated, leading to a four-lobe structure. Furthermore, for smaller circumferential domain sizes, the first higher harmonic of the fundamental wave length was the most dominant mode. This corresponds to the observations made in the discussion of the temporal spectra. Here, however, the main focus is on evaluating the effect of the dominant modes on the base pressure and the recirculation length. Thus, the mean streamwise velocity along the axis and the pressure coefficient along the base are scrutinized. Figure 10 shows the base pressure and streamwise axis velocity distributions for all cases at $Re_D = 3 \times 10^4$. The axisymmetric solution that served as initial condition for the DNS of all domain sizes is included for comparison. For the one-half-cylinder case, the recirculation length of the separated region is decreased to $z = 5.6$ vs 6.1 for the axisymmetric case. However, even more significant than the decrease in recirculation length is the drastic change of the shape of the profile within the recirculation region. Not only has the location of the maximum reverse velocity considerably moved downstream, its value has also strongly decreased. These differences are a consequence of the mixing of low-speed fluid contained in the recirculation region with the outer high-momentum fluid through the structures discussed earlier. The pressure distribution along the base, obtained from the one-half-cylinder calculation, is completely flat as opposed to the axisymmetric case, where a strong radial variation, with a pronounced maximum at the axis, is visible. The data from the DNS of the one-half-cylinder on a finer grid are included in Fig. 10 for comparison. The same result is obtained on both grids for the base pressure. Only a slight difference can be detected within the recirculation region ($z \approx 1.5$); however, the same recirculation length and roughly the same maximum reverse velocity are predicted.

For the one-quarter-cylinder case, the base-pressure coefficient is very similar to that found in the one-half-cylinder case, displaying only a slight radial variation. The data obtained from the one-quarter-cylinder calculation show an even shorter recirculation length. It is suggested that the structures generated in this case contain more energy, thus entraining more low-momentum fluid from the reverse-flow region. The location of the maximum reverse velocity is slightly farther upstream, albeit with roughly the same magnitude. Because of the similarities between the one-half- and the one-quarter-cylinder cases, it can be concluded that mode $k = 1$ only plays a minor role for the present flow conditions. The main effects that can be attributed to mode $k = 1$ are a short plateau in the streamwise axis velocity at $z \approx 1$ that can only be seen in the one-half-cylinder case and that causes a perfectly flat pressure distribution.

Scrutinizing the results obtained from the calculation of the one-sixth-cylinder verifies that the azimuthal modes $k = 2$ and 4 are the most relevant modes for this Reynolds number. Both modes are excluded in this case, and the recirculation length strongly increases, eclipsing even the value of the axisymmetric solution. The base-pressure distribution also exhibits a more pronounced radial variation, with the mean value being higher than the mean magnitude found for the larger domain sizes. In the simulations of the 1/8- and 1/16-cylinders the amplitude levels of the dominant modes are not large enough to modify significantly the mean flow or to generate any significant structures. Hence, these cases fail to reproduce the results of the one-half-cylinder case, that is, a flat pressure distribution along the base and a short recirculation region.

From the preceding results, it is not clear whether the main cause of the flat pressure profile on the base is the unsteadiness or the three dimensionality of the flow, that is, effects of higher azimuthal modes. To clarify this, an axisymmetric calculation at $Re_D = 4 \times 10^5$, a Reynolds number that is significantly larger than the threshold value for an absolute instability with respect to the axisymmetric mode,[28] was conducted that became highly unsteady. The mean pressure coefficient distribution along the base for the unsteady case is compared with the steady results from axisymmetric calculations at lower Reynolds numbers in Fig. 11. As for the steady lower-Reynolds-number cases, a strong radial distribution

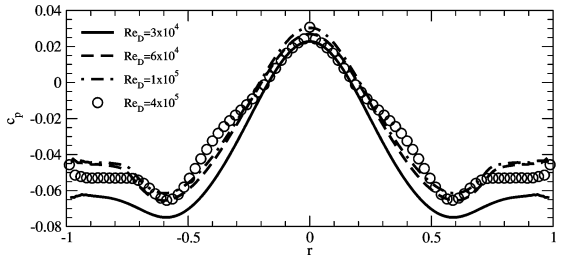

Fig. 11 Pressure coefficient on base obtained from axisymmetric DNS calculations for various Reynolds numbers, $M = 2.46$.

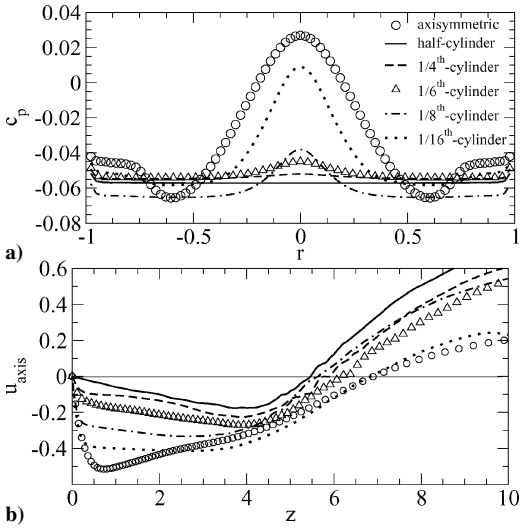

Fig. 12 All circumferential domain-sizes: a) time-averaged pressure coefficient and b) streamwise axis velocity; $Re_D = 6 \times 10^4$ and $M = 2.46$.

with a pronounced peak at the axis can be seen. The peak value is fairly constant for all cases, which can be attributed to the similar maximum reverse velocity at all Reynolds numbers and the same slope of the streamwise axis velocity at the base. The fact that the result from the highly unsteady axisymmetric calculation does not show any significant deviation from the steady cases demonstrates that the flat pressure distribution on the base, found for the three-dimensional DNS, is not caused by the axisymmetric mode. Therefore, the flat pressure distribution on the base must be a direct consequence of higher azimuthal modes.

The time-averaged streamwise velocity along the axis and the pressure coefficient along the base are compared for all cases at $Re_D = 6 \times 10^4$ in Fig. 12. In the one-half-cylinder case, the energetic large structures reduce the recirculation length by 24.4% compared to the axisymmetric calculation, that is, the mean reattachment point moves from $z = 6.9$ to 5.2. Note that the reduction of the recirculation length amounted to only 13.2% in the lower-Reynolds-number case. The pressure distribution along the base is entirely flat as at $Re_D = 3 \times 10^4$. The data from the one-quarter-cylinder case are very close to that of the one-half-cylinder case. Only a minimal radial variation of the base pressure can be observed. This implies that the effect of mode $k = 1$ on the mean flow becomes less significant as the Reynolds number is increased. The base-pressure profile obtained from the one-sixth-cylinder calculation only shows a marginal peak at the axis. However, the recirculation length is longer than for both the one-quarter-cylinder and the one-eighth-cylinder calculations, reconfirming that the structures generated by $k = 2$ and 4 are the most energetic, entraining a large amount of fluid from the recirculation region and thereby shortening the separated region. The streamwise velocity along the axis obtained from the one-eighth-cylinder case nearly coincides with that of the one-quarter-cylinder case for $z > 5$. However, in the recirculation region, the magnitude of the reverse flow is significantly higher. Compared to the lower-Reynolds-number case, the base-pressure profile of the one-eighth-

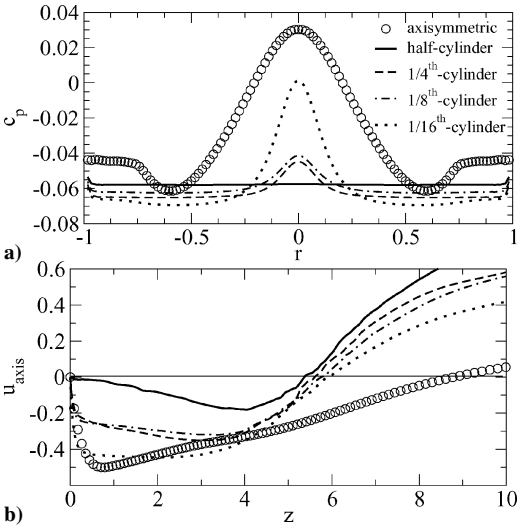

Fig. 13 All circumferential domain-sizes: a) time-averaged pressure coefficient and b) streamwise axis velocity; $Re_D = 1 \times 10^5$ and $M = 2.46$.

cylinder case is fairly flat. Only the result from the smallest domain size exhibits a very pronounced peak, approaching the solution of the axisymmetric calculation. The behavior observed here is in line with the findings for the lower-Reynolds-number case, namely, that modes with large wavelengths are mainly responsible for producing an entirely flat pressure distribution on the base.

The effect of the dominant structures on the recirculation length and the base pressure is compared for all cases at $Re_D = 1 \times 10^5$ in Fig. 13. As for the lower-Reynolds-number cases, in the one-half-cylinder calculation the pressure distribution along the base is entirely flat. A fast transition process, leading to energetic structures, is responsible for a dramatic decrease in recirculation length (the mean reattachment shifts from $z = 8.5$ to 5.3) and a strongly reduced reverse flow velocity within the recirculation region.

Unlike the lower-Reynolds-number cases, the results obtained from both the one-quarter-cylinder and the one-eighth-cylinder calculations are very similar to each other. The mean pressure coefficient is higher than in the one-half-cylinder case and a slight radial variation with a peak at the axis can be observed. The similarity in the data from the one-quarter-cylinder and the one-eighth-cylinder calculations implies that the flow pattern and the structures generated by the dominant modes of the respective calculation ($k = 4$ and 8) are similar. Furthermore, the mean reattachment location is considerably farther downstream, and the reverse flow maximum is much higher than in the one-half-cylinder case. The drastic differences that result from the elimination of mode $k = 1$ for these cases suggest that mode $k = 1$ is significant within the recirculation region for this Reynolds number.

As already indicated by the preceding results, the 1/16-cylinder case produces sufficiently energetic structures to reduce considerably the recirculation length. In fact, the mean reattachment point is located only marginally downstream of that of the two larger-domain cases, in spite of a significantly larger maximum reverse-flow velocity within the recirculation region. The pressure peak at the axis is more pronounced. However, in contrast to the lower Reynolds numbers, the deviation from the larger circumferential domain sizes is confined to a considerably smaller radial extent. As in the lower-Reynolds-number cases, it can be concluded that the long-wavelength modes, that is, $k = 1$ and 2, are essential in obtaining an entirely flat profile.

Overall, the most important observation is that when the azimuthal mode $k = 2$ was excluded, that is, in calculations with a circumferential domain size smaller than one-quarter-cylinder, an increase in the mean base pressure was observed. When the other dominant mode, $k = 4$ (one-sixth-cylinder and smaller than a one-eighth-cylinder cases), is deliberated eliminated the base pressure was increased even further. The knowledge gained from these calculations might be valuable in the pursuit to decrease base drag by

means of flow control. When the dominance of the naturally most important modes is decreased, a pressure increase at the base and, consequently, a drag reduction, could be accomplished. Preliminary evidence that methods can be devised to achieve this goal by exploiting and/or counteracting the instability mechanisms present in the flow was presented by Sandberg and Fasel.[36]

C. Turbulence Statistics

To obtain averaged turbulent quantities, the calculations were continued for at least six flow-through times using the converged running averages just discussed as mean flow. Side and end views of several turbulence quantities are shown in Figs. 14 and 15 for data obtained from the one-half-cylinder calculation. The sideviews of K, ε, and the turbulent shear stress $\langle u'v' \rangle$ illustrate that no significant fluctuations are present before roughly two radii downstream of the base. Furthermore, it can be observed that the highest activity is present on the inside of the shear layer, with the magnitudes of the respective quantities increasing in the downstream direction. Endviews for both K and ε at $z = 7$, downstream of the mean reattachment point, where the highest levels of most turbulent quantities were found, reflect the four-lobe structure of the wake. The four-lobe structure is a consequence of streamwise vortices generated by the dominant azimuthal modes $k = 2$ and 4 (Ref. 28). These vortices most likely generate small-scale structures, evidenced by the highest level of K and ε in the lobes, implying that the small-scale structures are a consequence of additional instabilities. The strong

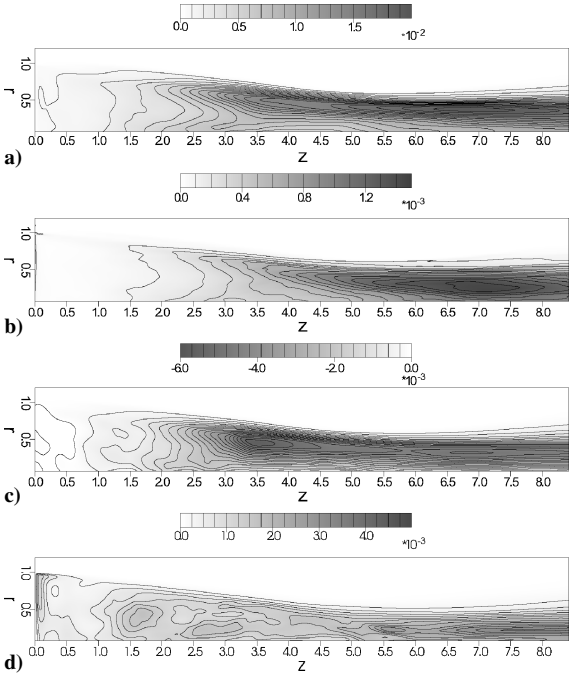

Fig. 14 Azimuthal average of turbulent statistics, side views for one-half-cylinder case: a) K, b) ε, c) $\langle u'v' \rangle$, and d) $\langle w'w' \rangle$; $Re_D = 3 \times 10^4$ and $M = 2.46$.

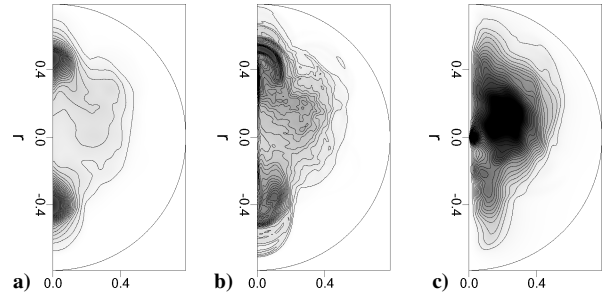

Fig. 15 Turbulent statistics, end views at $z = 7$ for one-half-cylinder case: a) K, b) ε, and c) $\langle w'w' \rangle$; $Re_D = 3 \times 10^4$ and $M = 2.46$.

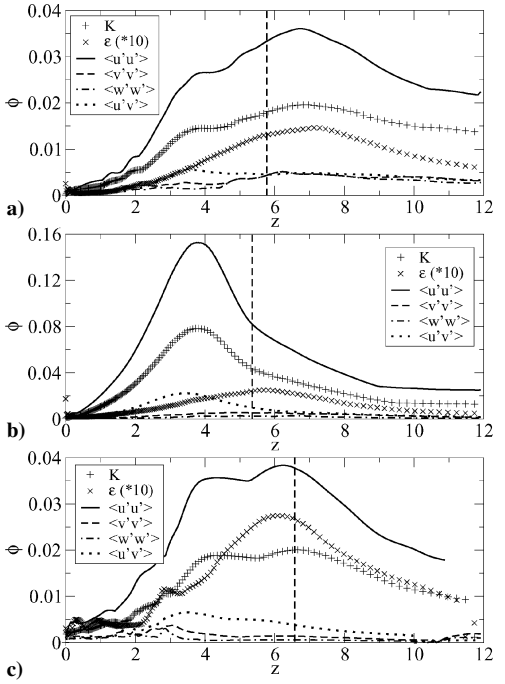

Fig. 16 Radial maxima of various averaged turbulent statistics over streamwise coordinate obtained for a) one-half, b) one-quarter, and c) one-eighth cylinder vertical dashed line denotes respective mean reattachment length; $Re_D = 3 \times 10^4$ and $M = 2.46$.

azimuthal variation of the turbulent quantities further suggests that when employing turbulence closures at higher Reynolds numbers, the transport equations for turbulence quantities ought to be solved fully three dimensionally. In addition, the large amplitudes of the azimuthal normal-stress component, $\langle w'w' \rangle$, seen in side and end views confirm that turbulent fluctuations in the azimuthal direction should not be neglected. Note that the use of symmetric Fourier transforms prohibit fluctuations across the $\theta = (0, \pi)$ plane, hence, $\langle w'w' \rangle >$ is zero there.

To quantify and find the streamwise location of the maximum values, the radial maxima of each variable over the streamwise coordinate are shown in Fig. 16. For reference, the mean recirculation length is denoted by the vertical dashed line. For better visibility, ε is multiplied by 10. The radial maxima of K, ε, and $\langle u_i' u_k' \rangle >$, are located downstream of the mean reattachment point. In contrast, the maximum of the most significant shear-stress component, $\langle u'v' \rangle$, is located upstream of the mean reattachment point, at $z \approx 3.5$. Because the shear-stress component can be related to the radial gradient of the mean streamwise velocity component, $\langle u'v' \rangle \sim \partial \bar{u} / \partial r$, this behavior can most likely be attributed to the decreasing shear-layer velocity gradient in the streamwise direction. The observations for the low-Reynolds-number transitional case are in contrast to the data obtained from the UIUC experiments.[37] In their case the maxima of most turbulence quantities were located upstream of the mean reattachment point.

For all circumferential domain sizes, $\langle u'u' \rangle$ is the dominant turbulent-stress component. The other two normal-stress components are fairly similar to each other in magnitude and shape, such that $\langle u'u' \rangle \gg \langle v'v' \rangle \approx \langle w'w' \rangle$. Therefore,

$$K = \tfrac{1}{2} \langle u'u' + v'v' + w'w' \rangle \approx \tfrac{1}{2} \langle u'u' \rangle \tag{6}$$

explaining the similar shapes of the K and $\langle u'u' \rangle$ profiles. K is roughly one order of magnitude larger than the turbulent dissipation rate ε. Also note that $\langle u'v' \rangle$ has its maximum within the recirculation region, with magnitudes significantly larger than those of $\langle v'v' \rangle$ and $\langle w'w' \rangle$ in that region. However, for both the one-half-cylinder and the one-quarter-cylinder calculations, the values of the two normal-stress components increase in the downstream direction, whereas the shear-stress component decreases, so that downstream of the mean

reattachment point $\langle v'v' \rangle \approx \langle w'w' \rangle \geq \langle u'v' \rangle$. The K and $\langle u'u' \rangle$ distributions both reach a plateau at the streamwise location where the shear-stress component reaches its maximum value in the one-half-cylinder and one-eighth-cylinder calculation, before increasing further toward their global maxima. A possible explanation for this behavior is that, once the flow has transitioned, the turbulence production remains fairly constant. Only when the flow becomes subjected to the strong streamwise pressure gradient in the reattachment region does the turbulence production increase significantly.

In the one-quarter-cylinder case, however, a striking difference can be observed. K and $\langle u'u' \rangle$ increase monotonically until attaining their global maxima noticeably upstream of the mean reattachment point. Their maxima coincide with the location of the maximum of $\langle u'v' \rangle$. The magnitudes reached at the peaks are significantly larger than for all other cases. A cause for this behavior might be that the transition process is more violent than for the other cases, immediately generating more energetic structures that lead to higher values in the turbulent statistics. This is consistent with the decreased recirculation length due to more energetic structures as discussed earlier.

Finally, the availability of the distribution of the turbulent dissipation rate is useful as another criterion for determining whether the calculation is well-enough resolved. The Kolmogorov length scale L_K was computed and compared with the grid spacing. For the one-half-cylinder case, the maximum value of ε was $\varepsilon \approx 0.0015$, resulting in $L_K = \mathcal{O}(10^{-3})$. Note from Fig. 14 that the location of this maximum is approximately at $(z, r) = (7, 0.25)$. The numerical grid resolution for the finer grid at this point is $\Delta z = 0.0524 = \mathcal{O}(10 \cdot L_K)$, $\Delta r = 0.01 = \mathcal{O}(L_K)$, and $r\Delta\theta = 0.25 \cdot \pi/128 = 0.00616 = \mathcal{O}(L_K)$. Hence, the numerical resolution in the radial and the azimuthal direction are on the order of the Kolmogorov length scale. In the streamwise direction, the grid spacing is roughly one order of magnitude larger than L_K, which is at the lower limit of what is considered adequate for resolving the relevant length scales. However, because the estimate for the Kolmogorov length scale is based on the maximum of ε, and the streamwise grid becomes finer approaching the base, the streamwise resolution is also considered to be sufficient. The same procedure was repeated for the two higher-Reynolds-number cases. Here, the grid resolution in the radial and azimuthal directions also appeared to be adequate.

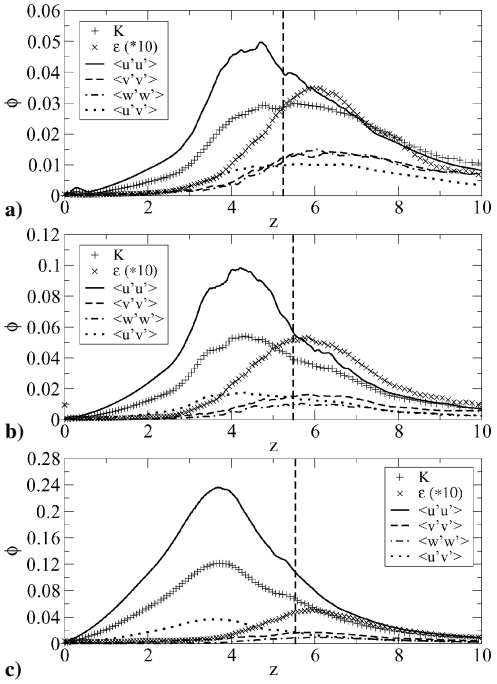

Fig. 17 Radial maxima of various averaged turbulent statistics over streamwise coordinate obtained for a) one-half, b) one-quarter, and c) one-eighth-cylinder; vertical dashed line denotes respective mean reattachment length; $Re_D = 1 \times 10^5$ and $M = 2.46$.

In the streamwise direction the resolution was at the lower limit of what is considered adequate for resolving the relevant length scales.

The radial maxima of turbulence quantities over the streamwise coordinate are shown for several cases at $Re_D = 1 \times 10^5$ in Fig. 17. In contrast to the lower Reynolds numbers, the radial maxima of K and $\langle u'u' \rangle$ are located upstream of the mean reattachment point for all cases. This is in agreement with the observations made by Herrin and Dutton[37] and constitutes further proof that the base flow at $Re_D = 1 \times 10^5$ is similar to the experiment at $Re_D = 3.3 \times 10^6$. The maximum dissipation rate can be found just downstream of the mean reattachment point; however, this quantity was not measured in the experiments and, therefore, no comparison can be made. In general, the values of all quantities are higher than at the lower Reynolds numbers, in particular the one-eighth-cylinder cases exhibit strongly increased amplitudes even exceeding those found for the larger domain sizes. As suggested earlier, this can most likely be explained by a large amount of energy being transferred directly to the most important modes. Because of the omission of modes by conducting calculations with smaller domain sizes, this energy cannot be redistributed to the modes excluded through nonlinear interaction and results in highly energetic structures.

V. Summary

DNS of supersonic base flows were conducted for several Reynolds numbers at $M = 2.46$. Simulations of different circumferential domain sizes were carried out to deliberately eliminate azimuthal modes. Thus, the effect of large-scale structures associated with particular azimuthal modes on the global flow behavior, in particular on the base pressure, could be evaluated. At $Re_D = 3 \times 10^4$, unstable modes intermittently lead to the generation of large-scale structures. It is suggested that the intermittency is a direct consequence of the large-scale structures interacting nonlinearly with the azimuthal mean flow, causing the basic state to intermittently become stable and unstable with respect to disturbances. For the 1/16-cylinder case, a viscous cutoff of the high wave numbers prevents linear growth of the higher azimuthal modes. In addition, the exclusion of the highly unsteady low-wave-number modes inhibits an energy cascade to the higher wave numbers, resulting in the absence of small-scale structures. For increasing Reynolds numbers, the viscous cutoff is shifted toward higher wave numbers. This is evidenced by the 1/16-cylinder case at $Re_D = 1 \times 10^5$, displaying a broad range of length and timescales. At both $Re_D = 6 \times 10^4$ and $Re_D = 1 \times 10^5$, all cases with a circumferential domain size larger than $0 \leq \theta < \pi/8$ do not exhibit intermittency. It is observed in temporal spectra that the frequencies found in the axisymmetric mode $k = 0$ can be related to the dominant higher modes present in the flow according to $(n, k) + (n, -k) = (2 \times n, 0)$. This can be confirmed by comparing results from different circumferential domain sizes with each other. A considerable amount of energy can be found in frequencies with $Sr_D \geq 1$, whereas maxima for lower azimuthal modes at low frequencies attest to the presence of large-scale structures in the flow. The temporal spectra also provide preliminary evidence that modes $k = 2$ and 4 might be the most significant azimuthal modes for the flow conditions investigated.

Time-averaged data illustrated that the structures present in the flow have a substantial effect on the mean flow, causing a decrease in recirculation length and base pressure compared to axisymmetric simulations. Furthermore, it was demonstrated that azimuthal modes with low wave numbers, and not the axisymmetric mode, are responsible for an entirely flat pressure distribution on the base. Furthermore, the simulations of domain sizes with decreased circumferential extent illustrated that the base pressure was increased when the most dominant modes were excluded. For $Re_D \leq 6 \times 10^4$, turbulence statistics revealed that the maximum values of all turbulence quantities, except the turbulent shear-stress component $\langle u'v' \rangle$, were located downstream of the mean reattachment point. At $Re_D = 1 \times 10^5$ the radial maxima of K and $\langle u'u' \rangle$ were located upstream of the mean reattachment point, similar to data obtained in the UIUC experiments. The Reynolds shear stress always exhibited a maximum upstream of the recompression due to the decreasing radial velocity gradient of the shear layer in the streamwise

direction. End views illustrate that a strong azimuthal variation of the turbulence quantities is present. Finally, the turbulence dissipation rate was used to estimate the Kolmogorov length scale, and it was determined that the spatial resolution of the calculations was adequate.

Acknowledgments

This work was supported by the U.S. Army Research Office under Grant DAAD 19-02-1-0361 #1. Thomas L. Doligalski served as Program Manager. Computer time for the direct numerical simulations on the Engineer Research and Development Center/Major Shared Research Center under Challenge project VI9ARONC11312C1D is acknowledged. We are grateful to Craig Dutton for providing the experimental data.

References

[1]Rollstin, L., "Measurement of Inflight Base Pressure on an Artillery-Fired Projectile," *Journal of Spacecraft and Rockets*, Vol. 27, No. 1, 1990, pp. 5, 6.

[2]Sahu, J., Nietubicz, C., and Steger, J., "Navier–Stokes Computations of Projectile Base Flow with and Without Mass Injection," *AIAA Journal*, Vol. 23, No. 9, 1985, pp. 1348–1355.

[3]Cortwright, E. M., and Schroeder, A. H., "Preliminary Investigation of Effectiveness of Base Bleed in Reducing Drag of Blunt-Base Bodies in Supersonic Stream," NACA Rept. RM E51 A26, March 1951.

[4]Reid, J., and Hastings, R. C., "The Effect of a Central Jet on the Base Pressure of a Cylindrical Afterbody in a Supersonic Stream," Aeronautical Research Council, Repts. and Memoranda 3224, London, Dec. 1959.

[5]Clayden, W. A., and Bowman, W. C., "Cylindrical Afterbodies at $M = 2$ with Hot Gas Ejection," *AIAA Journal*, Vol. 6, No. 12, 1968, pp. 2429–2431.

[6]Valentine, D., and Przirembel, C., "Turbulent Axisymmetric Near-Wake at Mach Four with Base Injection," *AIAA Journal*, Vol. 8, No. 12, 1970, pp. 2279–2280.

[7]Sahu, J., and Heavey, K. R., "Numerical Investigation of Supersonic Base Flow with Base Bleed," *Journal of Spacecraft and Rockets*, Vol. 34, No. 1, 1995, pp. 61–69.

[8]Mathur, T., and Dutton, C., "Base-Bleed Experiments with a Cylindrical Afterbody in Supersonic Flow," *Journal of Spacecraft and Rockets*, Vol. 33, No. 1, 1996, pp. 30–37.

[9]Mathur, T., and Dutton, C., "Velocity and Turbulence Measurements in a Supersonic Base Flow with Mass Bleed," *AIAA Journal*, Vol. 34, No. 6, 1996, pp. 1153–1159.

[10]Bowman, W. C., and Clayden, W. A., "Boat-Tailed Afterbodies at $M = 2$ with Gas Ejection," *AIAA Journal*, Vol. 6, No. 10, 1968, pp. 2029–2030.

[11]Bourdon, C. J., and Dutton, J. C., "Effects of Boattailing on the Turbulence Structure of a Compressible Base Flow," *Journal of Spacecraft and Rockets*, Vol. 38, No. 4, 2001, pp. 534–541.

[12]Bourdon, C. J., and Dutton, J. C., "Visualization of a Central Bleed Jet in an Axisymmetric, Compressible Base Flow," *Physics of Fluids*, Vol. 15, No. 2, 2003, pp. 499–510.

[13]Hubbartt, J. E., Strahle, W. C., and Neale, D. H., "Mach 3 Hydrogen External/Base Burning," *AIAA Journal*, Vol. 19, No. 6, 1981, pp. 745–749.

[14]Ding, Z., Chen, S., Liu, Y., Luo, R., and Li, J, "Wind Tunnel Study of Aerodynamic Characteristics of Base Combustion," *Journal of Propulsion and Power*, Vol. 8, No. 3, 1992, pp. 630–634.

[15]Demetriades, A., "Turbulence Front Structure of an Axisymmetric Compressible Wake," *Journal of Fluid Mechanics*, Vol. 34, 1968, pp. 465–480.

[16]Demetriades, A., "Turbulence Measurements in an Axisymmetric Compressible Wake," *Physics of Fluids*, Vol. 11, No. 9, 1968, pp. 1841–1852.

[17]Demetriades, A., "Turbulence Correlations in a Compressible Wake," *Journal of Fluid Mechanics.*, Vol. 74, 1976, pp. 251–267.

[18]Cannon, S., Champagne, F., and Glezer, A., "Observations of Large-Scale Structures in Wakes Behind Axisymmetric Bodies," *Experiments in Fluids*, Vol. 14, No. 6, 1993, pp. 447–450.

[19]Bourdon, C. J., and Dutton, J. C., "Planar Visualizations of Large-Scale Turbulent Structures in Axisymmetric Supersonic Separated Flows," *Physics of Fluids*, Vol. 11, No. 1, 1999, pp. 201–213.

[20]Bourdon, C. J., Dutton, J. C., Smith, K. M., and Mathur, T., "Planar Visualizations of Large-Scale Turbulent Structures in Axisymmetric Supersonic Base Flow," AIAA Paper 98-0624, Jan. 1998.

[21]Bourdon, C. J., and Dutton, J. C., "Visualizations and Measurements of Axisymmetric Base Flows Altered by Surface Disturbances," AIAA Paper 2001-0286, Jan. 2001.

[22]Sahu, J., "Numerical Computations of Supersonic Base Flow with Special Emphasis on Turbulence Modeling," *AIAA Journal*, Vol. 32, No. 7, 1992, pp. 1547–1549.

[23]Tucker, P., and Shyy, W., "A Numerical Analysis of Supersonic Flow over an Axisymmetric Afterbody," AIAA Paper, 93-2347, June 1993.

[24]Krishnamurty, V. S., and Shyy, W., "Study of Compressibility Modifications to the k–ε Turbulence Model," *Physics of Fluids*, Vol. 9, No. 9, 1997, pp. 2769–2788.

[25]Fureby, C., Nilsson, Y., and Andersson, K., "Large Eddy Simulation of Supersonic Baseflow," AIAA Paper 99-0426, Jan. 1999.

[26]Forsythe, J. R., and Hoffmann, K. A., "Detached-Eddy Simulation of a Supersonic Axisymmetric Base Flow with an Unstructured Solver," AIAA Paper 2000-2410, June 2000.

[27]Forsythe, J. R., Hoffmann, K. A., Cummings, R. M., and Squires, K. D., "Detached-Eddy Simulation with Compressibility Corrections Applied to a Supersonic Axisymmetric Base Flow," *Journal of Fluids Engineering*, Vol. 124, 2002, pp. 911–923.

[28]Sandberg, R. D., and Fasel, H. F., "Numerical Investigation of Transitional Supersonic Axisymmetric Wakes," *Journal of Fluid Mechanics* (submitted for publication).

[29]Sandberg, R. D., and Fasel, H., "Instability Mechanisms in Supersonic Base Flows," AIAA Paper 2004-0593, Jan. 2004.

[30]Sandberg, R. D., and Fasel, H., "A Flow Simulation Methodology for Compressible Turbulent Axisymmetric Wakes," AIAA Paper 2003-0267, Jan. 2003.

[31]Meitz, H., and Fasel, H. F., "A Compact-Difference Scheme for the Navier–Stokes Equations in Vorticity–Velocity Formulation," *Journal of Computational Physics*, Vol. 157, No. 1, 2000, pp. 371–403.

[32]Chung, Y. M., and Tucker, P. G., "Accuracy of High-Order Finite Difference Schemes on Nonuniform Grids," *AIAA Journal*, Vol. 41, No. 8, 2003, pp. 1609–1611.

[33]Lewis, H. R., and Bellan, P. M., "Physical Constraints on the Coefficients of Fourier Expansions in Cylindrical Coordinates," *Journal of Mathematical Physics*, Vol. 31, No. 11, 1990, pp. 2592–2596.

[34]Sandberg, R. D., "Numerical Investigation of Transitional and Turbulent Supersonic Axisymmetric Wakes," Ph.D. Dissertation, Dept. of Aerospace and Mechanical Engineering, Univ. of Arizona, Tucson, AZ, Dec. 2004.

[35]Sandberg, R. D., and Fasel, H., "Direct Numerical Simulations of Transitional Supersonic Base Flows," AIAA Paper 2005-0098, Jan. 2005.

[36]Sandberg, R. D., and Fasel, H., "High-Accuracy DNS of Supersonic Base Flows and Control of the Near Wake," *IEEE Proceedings of the Department of Defense Users Group Conference 2004 (DoD UGC 2004)*, Inst. of Electrical and Electronics Engineers, Los Alamitos, CA, 2004, pp. 80–88.

[37]Herrin, J. L., and Dutton, J. C., "The Turbulence Structure of a Reattaching Axisymmetric Compressible Free Shear Layer," *Physics of Fluids*, Vol. 9, No. 11, 1997, pp. 3502–3512.

C. Kaplan
Associate Editor